# ELSEVIER

#### Contents lists available at ScienceDirect

# Carbon





# Unraveling the role of boron dimers in the electrical anisotropy and superconductivity in boron-doped diamond

Michał Sobaszek<sup>a,\*</sup>, Soonho Kwon<sup>b</sup>, Tomasz Klimczuk<sup>c</sup>, Paweł P. Michałowski<sup>d</sup>, Jacek Ryl<sup>e</sup>, Bogdan Rutkowski<sup>f</sup>, Dongying Wang<sup>g</sup>, Xinwei Li<sup>g</sup>, Marc Bockrath<sup>g,\*\*</sup>, Robert Bogdanowicz<sup>a</sup>, William A. Goddard III<sup>b,\*\*\*</sup>

- <sup>a</sup> Gdańsk University of Technology, Faculty of Electronics, Telecommunications and Informatics, Department of Metrology and Optoelectronics, 11/12 Narutowicza Str., 80-233. Poland
- <sup>b</sup> Materials and Process Simulation Center, California Institute of Technology, 1200 East California Blvd., California, 91125, USA
- <sup>c</sup> Gdańsk University of Technology, Faculty of Applied Physics and Mathematics and Advanced Materials Centre, Department of Solid State Physics, 11/12 Narutowicza Str., 80-233, Gdańsk, Poland
- d Łukasiewicz Research Network Institute of Microelectronics and Photonics, Aleja Lotników 32/46, 02-668, Warsaw, Poland
- <sup>e</sup> Advanced Materials Center, Gdańsk University of Technology, Narutowicza 11/12, 80-233, Gdańsk, Poland
- f Faculty of Metals Engineering and Industrial Computer Science, AGH University of Krakow, Al. A. Mickiewicza 30, 30-059, Kraków, Poland
- <sup>8</sup> Department of Physics, The Ohio State University, Columbus, OH, 43210, USA

#### ARTICLE INFO

# Keywords: Superconductivity Metal-insulator transition Bosonic anomaly Electrical anisotropy Quantum mechanics Deuterium-rich plasma Boron-doped diamond

#### ABSTRACT

We use quantum mechanics (QM) to determine the states formed by B dopants in diamond. We find that isolated B sites prefer to form BB dimers and that the dimers pair up to form tetramers (BBCBB) that prefer to aggregate parallel to the (111) surface in the <110> direction, one double layer below the H-terminated surface double layer. These tetramers lead to metallic character (Mott metal Insulator Transition) with holes in the valence band near the  $\Gamma$  point and electrons in the BBCBB tetramer promoted band along the X direction. Our experiments find very significant anisotropy in the superconductivity for boron-doped diamond thin films prepared with Microwave Plasma Assisted Chemical Vapor Deposition using deuterium-rich plasma. This leads to much higher conductivity in the X direction than the Y direction, as predicted by the QM. This phase transition to the anomalous phase is linked with the emergence of boson quantum entanglement states behaving as a bosonic insulating state. These anisotropic superconducting properties of the diamond film might enable applications such as single-photon detectors. We expect that this formation of a dirty superconductivity state is related to the BBCBB tetramers found in our QM calculations.

#### 1. Introduction

The superconductivity in boron-doped diamond (BDD) is most remarkable. Investigation of the Metal-Insulator transition (MIT) in diamond [1] found that the doping sufficient to reach the metallic phase coincides with the doping necessary for superconductivity. Dubrovinskaia et al. [2] reported the BDD transition in the polycrystalline superconducting state at 2.4–1.4K. Subsequently, thick polycrystalline BDD films were investigated by Wang et al. [3], finding typical type-II superconductor behavior with a superconducting transition

temperatures  $T_c$  of 10 K at the transition onset and 8.3 K for zero resistance.

Boron-doped nanocrystalline diamond (B:NCD) is a granular material in which the occurrence of the metal-insulator and superconductor-insulator transitions appear to be strongly linked to granularity [4]. The granularity parameter can often be controlled through various synthesis techniques, offering a test bed for various theoretical models developed to describe granularity in transport. The B:NCD synthesized by plasma-assisted CVD was studied by Nesladek et al. [5], who found the superconductive transition at ~1.66K, similar to B-doped epitaxial

E-mail addresses: micsobas@pg.edu.pl (M. Sobaszek), bockrath.31@osu.edu (M. Bockrath), wag@caltech.edu (W.A. Goddard).

<sup>\*</sup> Corresponding author.

<sup>\*\*</sup> Corresponding author.

<sup>\*\*\*</sup> Corresponding author.

diamond. Gajewski et al. reported  $T_c \sim 2K$  for the MIT with critical boron concentrations in the range from  $2\cdot 10^{20}$  up to  $3\cdot 10^{20}$  cm<sup>-3</sup> [6]. Furthermore, Takano et al. found the MIT around  $3\cdot 10^{20}$  cm<sup>-3</sup> [7]. In addition to the MIT, the fraction of (111) facets and the optimal grain size is vital to superconductivity in boron-doped diamond. We conclude that these two properties are correlated, resulting in an increased fraction of (111) facets with decreasing grain size [4,8]. The effects of granularity are usually expected to be most significant at temperatures below the intergranular single electron tunnel rate due to subtle host quantum interference effects, including modifications to the weak localization correction to conductivity [9]. Lerner, Varlamov and Vinokur (LVV) suggested a characteristic scaling scheme for granular superconductors that is based on the evolution of the temperature dependent Ginzburg-Landau coherence length driven by inter and intra-grain coupling [10].

The above observations indicate that phase slips and metastability can play a significant role in the superconductivity of boron-doped nanocrystalline diamond. Klemencic *et al.* described phase slip as a localized disturbance in the coherence of a superconductor that allows an abrupt  $2\pi$  phase shift [11]. We suggest that the intrinsic Josephson junction is tied to phase slips.

Various effects influencing superconductivity have been reported in the literature including bosonic anomalies, boron-defects, Yu-Shiba-Rusinov bands, and crystallite geometry. Zhang et al. reported anomalous resistance peaks that result from confinement and coherence effects in the presence of intrinsic and extrinsic granularity [12]. Ashcheulov et al. investigated specific boron defects on BDD conductivity and found that when the concentration of B is low, single substitution defects are predominant [13]. In contrast, as the B concentration increases, more complex defects occur, mainly B-dimers and we suggest BBCBB tetramers. Next, we consider the Yu-Shiba-Rusinov bands where individual local magnetic moments interacting with superconducting electrons give rise to in-gap localized states that can influence the superconductivity in BDD [14]. Furthermore, in granular systems, such as polycrystalline diamond, the crystal grain geometry can play a crucial role in the superconducting properties. BDD measured in-plane and out-of-plane reveals anomalous anisotropy induced by the presence of columnar grain boundaries and intragrain twin boundaries that lie in the out-of-plane direction [15].

Substituting hydrogen with deuterium results in such physicochemical differences as enhanced boron doping efficiency [16], richness of the (111) phase, and lack of degenerative effects on grains, a well-known phenomenon [17]. During the diamond synthesis various of boron complexes are created such as B, BB, BBB, B4V, BBCBB and so on [18–20].

In this paper we use quantum mechanics (QM) to ascertain the states created by B dopants in diamond. We find that isolated B sites prefer to form BB dimers, which are 0.21 eV more stable. Moreover, we find that these dimers prefer to come together to create tetramers (BBCBB), which are much more stable by 0.96 eV. We find that the BBCBB tetramers strongly prefer to cluster parallel to the (111) surface in the  $<\!110>$  direction, situated one double layer beneath the H-terminated surface layer. We show that these tetramers lead to a Mott Insulator transition to a conducting state, making them presumably responsible for the superconductivity. The orientation of the tetramer near the surface leads to anisotropy in the in-plane  $R_{XX}$  and  $R_{YY}$  dependence of the resistive superconducting, which is consistent with and explains our experiments.

To the best of our knowledge the anomalous anisotropy in superconductivity measured in various directions of the in-surface planes and predicted from our QM theory has not been reported previously.

# 2. Experimental

*Diamond growth:* The deuterium or hydrogen boron-doped diamond films were deposited on p-type (100) silicon substrates (1  $\times$  1 cm). The substrates were cleaned in acetone in an ultrasonic bath for 5 min; then

they were washed in 2-propanol. The substrates were then sonicated in a water nanodiamond suspension (NanoAndo, Japan). The  $\rm D_2/CH_4$  gas mixture was 1 % vol. With an overall gas flow of 300 sccm. We used a temperature of 700 °C, a pressure of 50 Torr (6.7 kPa), and  $P_{MW}=1300$  W. Diborane ( $\rm B_2H_6$ ) was used as the boron source. The boron doping level expressed as the [B]/[C] ratio in the gas phase was set to 10K ppm. The growth time of BDD<sub>D</sub> films was 6 h, producing microcrystalline films with an average thickness of 650 nm.

Characterization (XPS, SEM, TEM): High-resolution X-ray photo-electron spectroscopy (XPS) studies were carried out on an Escalab 250 Xi from Thermofisher Scientific. The spectroscope is equipped with an Al K $\alpha$  source. The pass energy was 15 eV, and the spot size diameter was 650  $\mu m$ . Charge compensation was controlled through the low-energy electron and low energy  $Ar^+$  ions emission by means of a flood gun (emission current 150  $\mu A$ , beam voltage 2.1 V, filament current 3.5 A). Deconvolution was processed using implemented Avantage software (Thermofisher Scientific).

An FEI Quanta FEG 250 Scanning Electron Microscope (SEM) with  $10~\rm kV$  beam accelerating voltage, SE-ETD detector (secondary electron - Everhart-Thornley detector) and high vacuum mode (pressure  $10^{-4}~\rm Pa$ ) was used.

Transmission– and scanning-transmission electron microscopy (TEM and STEM, respectively) investigations were performed with probe Cs corrected Titan<sup>3</sup> G2 60–300 of Thermofisher Scientific, equipped with Gatan GIF Quantum system. Selected area electron diffraction (SAED) patterns were solved using JEMS software from JEMS-SWISS.

The x-ray diffraction at room temperature was carried out using Bruker D2 Phaser diffractometer with  $CuK\alpha$  radiation.

Electrical: Transport and Hall effect measurements were performed on a Quantum Design Physical Property Measurement System (PPMS). The electrical resistivity was measured by a conventional four-probe method, in which small diameter Pt wires (50  $\mu$ m) were attached to samples cut in to 5 by 5 mm, using conductive epoxy (Epotek H20E). A sample with contacts was annealed at 120 °C for 1 h in a chamber furnace. Data were collected from 1.9 to 300 K under zero field and in magnetic fields up to 0.5 T. The samples were measured in RXX and RYY direction. Additional transport measurements were performed in pumped He4 and He3 refrigerators. Data were collected via standard DC measurement techniques using SR830 lock-in amplifiers, Keithley 2400 source meters, and SR560 preamplifiers. Data were collected from 1.5 to 2.4K under zero field and in magnetic fields up to 1 T. The samples were measured in RXX and RYY direction (Fig. S1). The Ohmic contact was fabricated by platinum wire bonded with silver paste.

Regardless of the configuration being tested, the cleaved samples remained the same for electrical testing (see SI). Each configuration had one edge distanced from the sample break, along the crystalline axis of the silicon <100>. Additionally, the edges of the cleaved samples were slightly ground and polished to avoid short circuits.

*Raman spectroscopy:* The investigation of the molecular composition of the electrodes was carried out by means of Raman spectroscopy. A Horiba LabRAM ARAMIS Raman confocal microscope ( $100 \times /0.95$  objective, 50  $\mu$ m of confocal aperture) equipped with a 532 nm diodepumped solid-state (DPSS) laser was used.

SIMS: The measurements were performed with the CAMECA IMS SC Ultra instrument. Before the measurement, a thin gold layer ( $\sim$ 50 nm of thickness) was deposited on the sample. Cesium ions with moderate energy (2 keV) and high incident angle (80°) were used to polish any irregularities of the sample forming a flat surface. The exact details of the ion polishing procedure are presented elsewhere [21]. Cesium primary beam with ultra-low impact energy (100 eV), high incident angle (75°), moderate intensity (6 nA), and size (10  $\mu$ m) was used in the depth profiling mode. For lateral imaging intensity and size were reduced to 8 pA and 0.8  $\mu$ m, respectively. In both modes, detector polarity was altered for each data point and the relevant species were registered as C $^-$ , CB $^+$ , CsB $^+$ 2 signals. Positive ions were point-to-point normalized to the Cs $^+$  signal. The boron signal was additionally calibrated

based on a sample with known B concentration.

Computational details: We carried out spin polarized DFT calculations using the Vienna ab initio simulation package (VASP ver. 5.4.5) [22,23]. Electron exchange and correlation were treated within the generalized gradient approximation (GGA) [24] in the form of the PBE functional, including the D3 correction for London Dispersion (van der Waals attraction) [25]. The interaction between the ionic core and the valence electrons was described by the projector-augmented wave (PAW) method [26]. We used a plane-wave basis set with an energy cutoff of 500 eV. The convergence criteria for the electronic structure and the atomic geometry were  $10^{-6}$  eV and 0.01 eV/Å, respectively. We employed a  $2 \times 2 \times 2$  supercell of the conventional cubic unit cell of diamond (64 atoms) for screening various defect types, and a  $4 \times 4 \times 4$ supercell of the primitive cell of diamond (128 atoms) for band structure calculations. The Brillouin zone was sampled using the  $6 \times 6 \times 6$  and 4× 4 × 4 Monkhorst-Pack grid for the two supercell systems, respectively [27].

#### 3. Results and discussion

#### 3.1. Characterization

The Raman spectra provide a fast and noninvasive tool to determine boron doping level in diamond film, especially in highly doped film. In order to gain additional hints for the origin of the surprising anisotropies observed, we carried out Raman spectroscopy experiments showing strong bands at 1312 cm<sup>-1</sup> in the zero-phonon zone (Fig. 1a). This sp<sup>3</sup> peak is strongly asymmetric, which we attribute to the Fano effect due to interference between the scattering by the zone-center phonon line coupled to scattering by an electronic continuum [28–30]. Next, we attribute two peaks located at 480 cm<sup>-1</sup> and 1212 cm<sup>-1</sup> to boron doping. These two peaks arise from boron dimers (or tetramers) but involve coupling to C vibrations and B–C vibrations which were investigated in work by Ashcheulov et al. [18] and Niu et al. [19]. When boron-doping increases the more complex defects (mainly B dimers) accompanied by a larger deformation of the lattice are set [18]. Furthermore, according to the literature, these two broad bands correspond to maxima in the

phonon densities of the states [31]. Secondly, we can estimate the boron concentration from the peak located at 480 cm $^{-1}$  [32,33], which leads to  $8.68\cdot10^{20}$  cm $^{-3}$ , as in our previous investigation [34].

The inset of Fig. 1a shows the deconvoluted Raman spectra using the Breit-Wigner-Fano function (see Eq. (1)), which affirms Fano-shaped peaks located ca. 480 cm<sup>-1</sup>, 1212 cm<sup>-1</sup>, and 1312 cm<sup>-1</sup> marked as 1, 2 and 3, respectively [30,35].

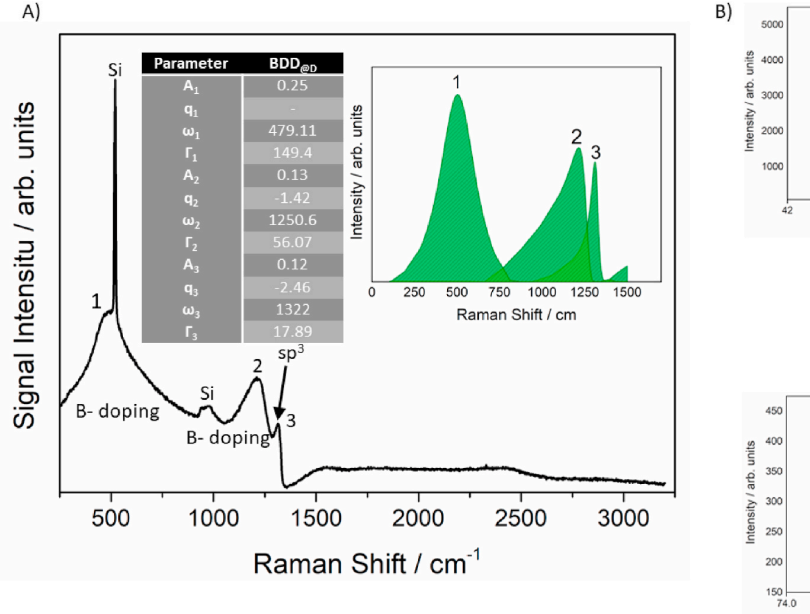
$$F_i(\omega) = rac{A_i imes \left(q_i + rac{\omega - \omega_i}{\Gamma_i}
ight)^2}{1 + \left(rac{\omega - \omega_i}{\Gamma_i}
ight)^2}$$
 (1)

In Equation (1),  $A_i$  is the amplitude of the Fano-shaped peaks,  $q_i$  is the asymmetric parameter,  $\omega_i$  is the width, and  $\Gamma_i$  is the position of the lines.

The fitting parameters are shown in inset of Fig. 1a. The peak associated with boron doping located at  $1212\,\mathrm{cm}^{-1}$  has an asymmetry factor  $q_2=-1.42$ , and the zero-phonon line attributed to  $\mathrm{sp}^3$  diamond has an asymmetry factor  $q_2=-2.46$ , which indicate a high incorporation of boron atoms in the diamond film/lattice [35]. We emphasize that the Raman spectra do not exhibit significant amounts of  $\mathrm{sp}^2$  character or C-H/C-D stretching bonds.

The crest-like grain boundaries of (111) and (220) microfacets that constitute the BDD<sub>D</sub> electrode surface, which we find to be dominated by nearly flat and crystalline edges of (111) microfacets. The BDD<sub>D</sub> films exhibit two main X-ray diffraction (XRD) peaks originating from (111) and (220) reflections, observed at  $2\theta=44$  and 75.5, respectively (see Fig. 1b). The (111) plane predominates, which is crucial since this plane is dramatically promoted by incorporation of boron atoms [36–38]. For a randomly oriented polycrystalline diamond powder, the theoretical value of the  $I_{(220)}/I_{(111)}$  ratio is 0.25, according to ASTM powder diffraction data. We find a  $I_{(220)}/I_{(111)}$  ratio for BDD<sub>D</sub> of 0.09, indicating that the texture of the BDD<sub>D</sub> is along the <111> direction.

Our XPS analyses examined the binding energy range of C1s (Fig. 2a) and B1s (Fig. 2b) peaks. The surface chemistry of BDD<sub>D</sub> shows an increased amount of boron in the BDD film structure. The amount ranges around 1 at.%, distributed among four different component types. According to the literature and our own experience on similar materials,



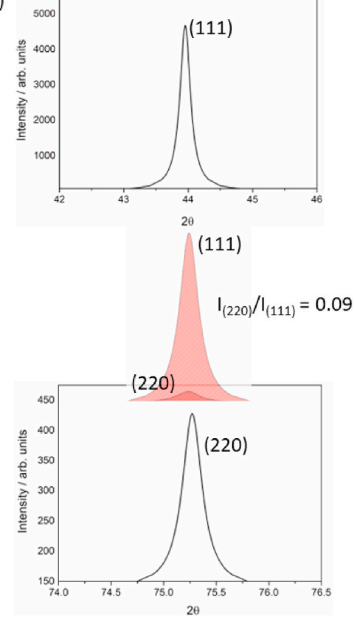


Fig. 1. a) Normalized raw Raman spectra of the BDD<sub>D</sub> electrode; inset shows deconvoluted Raman spectra using the Breit-Wigner-Fano function with fitting parameters; a) XRD spectra recorded for (111) and (220) phases and the  $I_{(220)}I_{(111)}$  ratio.

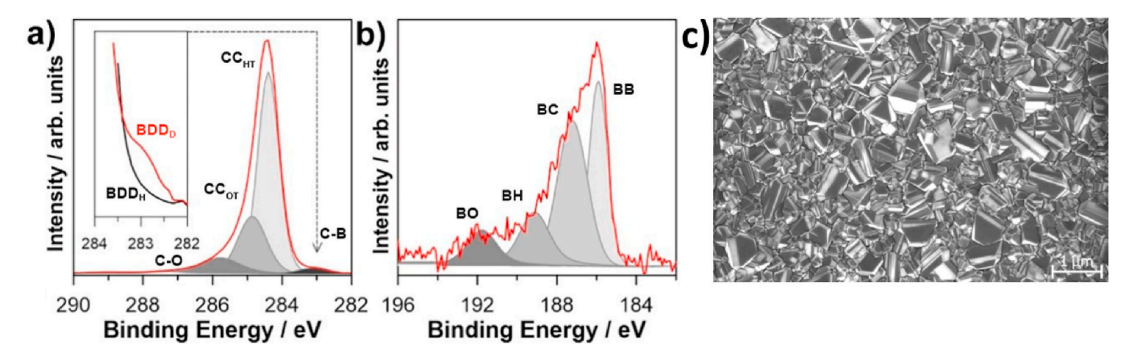


Fig. 2. High-resolution XPS spectra for a) C1s and b) B1s peak energy range with imposed spectral deconvolution; c) SEM micrograph for BDD<sub>D</sub>.

the two most prominent peaks originate from the B-B dimer (at 185.9 eV) and  $\rm B_4\text{-}C$  tetramer (at 187.7 eV) [39–41]. Indeed (vide infra) our QM finds that the most stable B clusters are the BB dimer and the t-t-BBCBB tetramer, consistent with the XPS analysis. Two smaller components may correspond to different other B containing clusters [42,43]. Significantly enhanced boron dopant concentrations are also observed in the C1s peak C-B, whose intensity increased six times. These XPS studies corroborate our Raman spectroscopy observations. A secondary effect due to higher boron incorporation is that the BDD\_D electrode becomes more prone to surface oxidation. This effect is manifested through the increased share of to surface hydroxyl-terminated BDD grains, which increase nearly four times.

It has been demonstrated previously that the propensity to oxidation is clearly correlated with BDD crystallographic texture [44–46]. Fig. 2c reveals the structure and size of the BDD<sub>D</sub>. The SEM micrograph reveals significantly altered crystallographic orientation of surface BDD grains, which we further examined with XRD studies. The BDD<sub>D</sub> electrode surface is dominated by nearly flat and even crystallite edges of (111) microfacets. Moreover, defects in the diamond crystal structure are visible as characteristic "steps" on the microfacets.

Measurements performed with gold capping layers at high incident angles are self-flattening and thus no issues with inhomogeneous sputtering of a sample with complex topography can be observed [47]. Thus a depth profile (Fig. 3) shows a realistic distribution of all measured species in the sample. For the first  $\sim\!20$  nm only the gold capping layer is sputtered which contains some minor contaminants that are reflected as low-intensity carbon signal. For the next  $\sim\!65$  nm carbon signal rapidly increases (it reflects the top part of the film with high roughness) and becomes stable after reaching the bulk of the layer. Boron distribution is very homogenous for the whole sample and the average concentration is

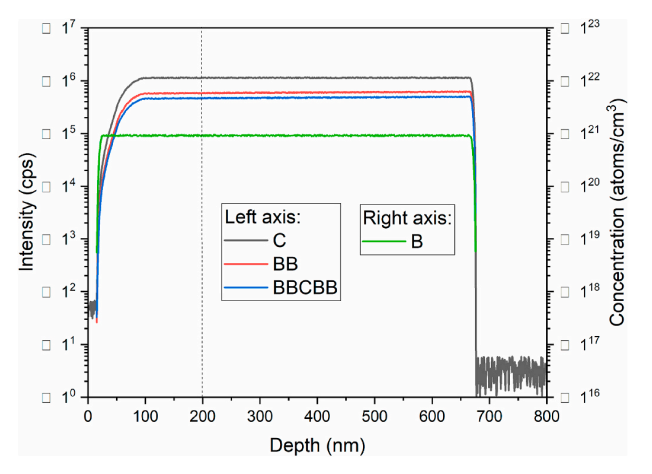


Fig. 3. Depth profile of distribution of B and B-dimers in BDD<sub>D</sub> sample.

8.98 x 10<sup>20</sup> atoms/cm<sup>3</sup> which is agreement whit Raman results.

For the dimer and tetramer signals (denoted as BB and BBCBB) it is important to emphasize that for such ultra low impact energy (100 eV) SIMS provide qualitative information about the chemical state of the sample, i.e. complex signals (consisting of more than one atom) can only be registered if particular species have been covalently bonded prior to the measurement [48]. Thus, the presence of these signals is direct evidence that such dimers and tetramers are present in the sample.

Moreover, at the depth of 200 nm (marked with a dashed line), the measurement has been switched to the imaging mode. Fig. 4 presents a lateral distribution of C, B, BB and BBCBB signals from  $30\times30~\mu m^2$  area. It can be immediately noted that monoatomic signals are evenly distributed whereas for BB and BBCBB signals a clear pattern similar to a stained glass can be observed. Importantly, the pattern is identical for both signals even though BB signal has a better signal-to-noise ratio which is natural since the intensity of this signal (cf. depth profile presented in Fig. 3) is higher.

The lateral resolution of the CAMECA IMS SC Ultra instrument is mostly governed by the size of the working spot (0.8  $\mu m)$  which causes the artificial blurring of smaller features. However, the pattern observed in Fig. 4 closely resembles the size and distribution of crystallites observed on SEM micrograph (cf. Fig. 2c). Thus it can be interpreted that the SIMS analysis reveals that the formation of dimers and tetramers predominantly takes place at the grain boundaries.

This conclusion can be further corroborated by the analysis of BB and BBCBB signals presented in the depth profile (cf. Fig. 3). Their intensity is not constant and the relative increase for both signals is identical and equals about 10 % when points at 100 and 650 nm are compared. Given that the grain boundary density is slightly higher close to the substrate and dimers and tetramers are predominantly formed at grain boundaries however, if the dimers will be located shallowly in the crystallite, the lateral image will be exactly the same.

#### 3.2. Anomalous anisotropy in superconductivity

To characterize the electrical transport properties of the BDD<sub>D</sub>, two sets of samples were measured on two independent fridge systems (Fig. 5 and Fig. S1). Fig. 5 shows the thermoresistance R(T) measured in the temperature range of 1.4–2.4 K at magnetic fields ranging from of 0–0.5T. The measurements in the  $R_{\rm XX}$  (Configuration I) direction and the  $R_{\rm YY}$  (Configuration II) direction are shown on Fig. 5a and b, respectively. In Configuration I at high temperatures the resistivity shows semi-conducting behavior. At lower temperatures the current shows a clear metal – insulator transition with current flowing through a fully superconducting (SC) channel. In both cases the measured  $T_{\rm c}$  is  $\sim\!2.0{\rm K}$  for Configuration I.

The obtained  $T_c$  result of ~2K aligns with literature data, considering that the layers are relatively thin (~650 nm). The  $T_c$  results for thin layers, ranging from 150 nm to 800 nm, are between 1.66K and 3.1K [49–52]. An intriguing case is the nanocrystalline diamond layer studied

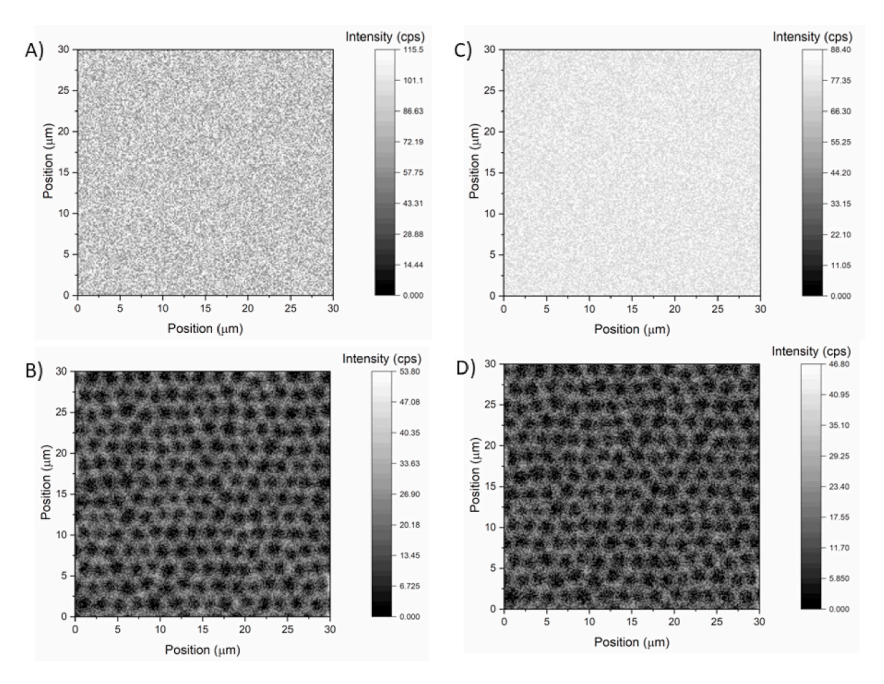


Figure 4. Lateral distribution for A) Carbon, B) B atoms, C) B-B dimer and D) BBCBB dimer.

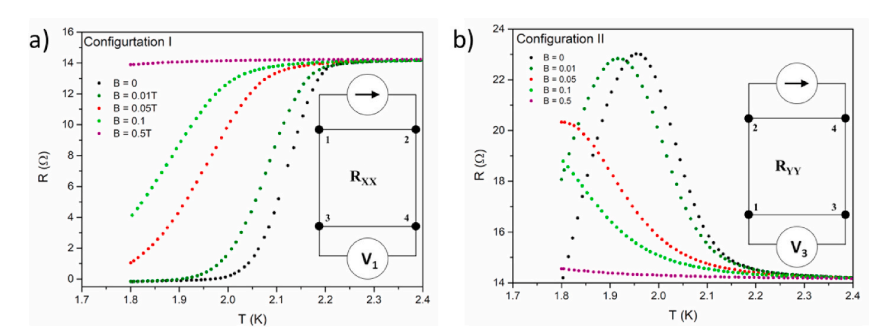


Fig. 5. The resistance, R(T). of heavily boron-doped polycrystalline diamonds synthesized with the rich-deuterium plasma in the MWCVD method, (a) superconducting transition near 2.0K for B = 0, (b) anomalous R(T) peak diminishes with increasing magnetic field. Thus, for B = 0.5T the resistance is nearly isotropic.

by G. Zhang et al. [49], where the authors achieved a  $T_c$  of approximately 2K with a very high doping level of  $7.3 \cdot 10^{21}$  and a significant predominance of the (111) phase.

Analyzing the works summarized in Table S1, higher  $T_c$  values (>4K) are reported for microcrystalline layers with significant thicknesses ranging from 60  $\mu$ m to 300  $\mu$ m. These layers are predominantly composed of mixed crystallographic phases such as (111), (220), or (113) [3,53,54]. These findings suggest that thicker microcrystalline layers with mixed crystallographic orientations can achieve higher Tc values, highlighting the importance of both layer thickness and crystallographic phase composition in determining superconducting properties.

Configuration II exhibits anomalous anisotropy in the superconductivity, resulting in a drastic increase of resistivity with decreasing temperature, and then a significant drop for B=0 and  $0.01\ T.$  In the perpendicular direction the current flows through a series of SC-normal metal/semiconductor junctions. When a SC gap forms, resistance appears at the SC-N junction as the quasiparticles carrying charge in the N state (electrons - fermions) different from those in the SC state (Cooper pair - composite bosons). Since the SC coherence length increases upon cooling from  $T_{\rm C}$  to 0K, Cooper pairs must at some point be able to

essentially tunnel through the junction since their coherence length is of the order of the separation of SC layers. At this point the resistivity drops (see Table 1).

#### 3.3. Quantum mechanics predictions for boron containing defects

To understand which boron defects are present and the role they might play, we performed Density Functional Theory (DFT) calculations at the PBE-D3 level to describe B-doped diamond. We constructed various  $B/V_C/H$  defect complexes in a  $2\times 2\times 2$  supercell structure of the conventional diamond lattice (64 atoms). For the carbon vacancy ( $V_C$ ) case, we saturated all adjacent undercoordinated C atoms with H atoms. We considered various boron-clusters, including BB, BCB, BV<sub>C</sub>B, BBB, BBCBB, B<sub>4</sub>V<sub>C</sub>, B<sub>4</sub>C and BBV<sub>C</sub>BB. We take the formation energy of the substitutional B defect in diamond as reference (0 eV) [55]. The calculated energy of formation for each defect case is shown in Table 2 along with spin states.

Starting with defects involving two boron atoms, we predict that the BB dimer (Fig. 6a) has a formation energy of -0.21 eV with respect to two single B substitutions. This agrees with our XPS experiment where B-B peaks are prominent. In this structure, each B has three single B-C

Table 1 Chemical composition on the surface of  $BDD_D$  electrode (in atomic %), based on deconvolution of the XPS spectra.

chemical state	C1s				B1s			
	C-C <sub>HT</sub>	C-C <sub>OT</sub>	С-ОН	С-В	В-В	B <sub>4</sub> -C	B-C <sub>3</sub>	B-C <sub>2</sub> O
BE/eV	284.4	284.9	285.7	283.3	185.9	187.7	188.3	191.5
$BDD_D$	57.3	27.0	11.1	3.6	0.3	0.5	0.1	0.1

**Table 2**DFT predicted formation energy of the various clusters relative to an isolated B site.

- ·		-f				
Boron cluster		E <sup>f</sup> [eV]				
		S = 0	S=1/2	S = 1	S = 3/2	
	$\begin{array}{c} BB \\ BCB \\ BV_cB \end{array}$	-0.21 $-0.08$ $0.80$		0.58 0.28		
Q	BBB t-t-	-0.96	-0.04	-0.32	0.08	
	BBCBB BBV <sub>c</sub> BB	2.01				
	0					
	~					
Tetrahedral	$B_4V_C$	-0.30				
	B <sub>4</sub> C	-0.40				

bonds with  $d_{B\cdot C}=1.53$  Å while the BB interaction is weak with  $d_{B\cdot B}=1.95$  Å. This configuration leads to a singlet state with no unpaired spin on any atom. The band structure of the BB dimer (with 1.6 at % of B) shows that it remains an insulator, with an excitation energy to the empty impurity band of 1.20 eV at the  $\Gamma$  point (Fig. 6c).

Much more favorable is to link two BB dimers through an in-between C atom, leading to the most favorable B defect complex, t-t-BBCBB (Fig. 6b). Here t-t indicates that both B-C dihedral angles are trans (180°). We calculate that t-t-BBCBB has a formation energy of -0.96 eV relative to four single site B sites. The t-t-BBCBB defect is oriented along the <110> direction. The coupling in t-t-BBCBB does not induce a significant structural deformation from the local B-B moiety (except a slightly shorter B-B distance of 1.92 Å)

slightly shorter B-B distance of 1.92 Å). The Bader charge analysis [J. Comp. Chem. 28, 899-908 (2007)] of t-t-BBCBB predicts one electron transfer per B-C bond leading to no valence electron on B and -1 net charge on bonded carbon and -2 for the central carbon (Fig. S2). To define the dipole direction of this defect, we compared the energies with two opposite electric field along the surface normal (Fig. S3) and found that the dipole direction is toward two outer B as indicated in Fig. 6b.

The band structure for t-t-BBCBB with 3 at % of B (Fig. 6d) shows two impurity bands that are mostly dominated by B character. The upper band ranges from 1.39 to 1.96 eV above Fermi level while the lower band drops below the Fermi energy and ranges from -0.7 to +0.61 eV. Therefore, the BBCBB defect leads to metallic character (the Mott Insulator Transition and presumably superconductivity) with 0.06 holes in the valence band near the  $\Gamma$  point and 0.06 electrons at the X point. Thus, BBCBB leads to the Mott metal-insulator transition and presumably the superconductivity. By rotating k-point path by  $120^{\circ}$  along [111] direction (Fig. S4), we examined the orientation-dependent band structure with respect to BBCBB direction. Compared to that of BB dimer

(Fig. S5), we found that the Fermi level crossing occurs along the [110] direction along the t-t-BBCBB (Fig. S6). This implies a directional dependent conductivity, leading to anisotropic conductivity.

In addition to the all-trans t-t-BBCBB cluster, other configurations are.

- the gauche-trans BBCBB (g-t-BBCBB) conformation, with a dihedral angle ∠BCBB = 62.73° at an energy 0.30 eV higher than t-t-BBCBB state and,
- the two gauche-gauche BBCBB (g-g-BBCBB) conformations have an energy 0.78 eV above t-t-BBCBB for  $g^+$ -g-( $\angle$ BCBB = 72.51°) and 0.61 eV above for  $g^-$ -g-( $\angle$ BCBB = 55.54°),
- separating the two BB dimers by an extra C to form (BBCCBB) increases the energy by 0.67 eV,
- BBV<sub>C</sub>BB has a quite high formation energy of +2.01 eV.

None of the other BC clusters listed in Table 2 are expected to play an important role.

Based on these results, we expect that the CVD growth process initially forms BB dimers in addition to isolated B monomers and that the dimers couple during deposition and growth to form t-t-BBCBB defects oriented in a <110> direction parallel to the surface and in the second double layer from the deuterated surface double layer. Literature studies show that many of the boron atoms incorporated into the diamond lattice do *not* act as acceptors, with even 90 % of the impurities being electrically inactive [13,56]. This is consistent with our calculations for the isolated B atom and BB defects, but *not* for t-t-BBCBB.

Furthermore, the stability of the BBCBB defect likely promotes segregation into highly defective regions of the material or within inclusions. Considering the high correlation between the MIT and the (111) surface [5,11], we calculated the relative energy of this BBCBB with different locations and orientations near the surface. As shown in Fig. 6e–j, we find that the t-t-BBCBB strongly prefers to be in the double layer just below the H-terminated surface double layer (Fig. 6f). Rotating the tetramer by 180° along the <110> axis so that its dipole opposite to the surface showed negligible energy difference (Fig. 6i). Compared to the BBCBB defect with angle of 35.7° to the surface normal (Fig. S7), the BBCBB shows a strong preference (by 0.2–0.5 eV) for parallel orientation to the (111) surface. Thus, BBCBB has a strong interaction with the (111) surface.

We also investigated the interaction between the two tetramers using 6x4 surface model with 4 bi-layers (240 atoms). We found that the lowest energy configuration is a periodic linear chain of composition (BCB)<sub>n</sub> along an <110> axis (Fig. S8), maximizing the number of BCB moieties. The other configurations in the 2nd surface bilayer are all higher in energy regardless of different defect and dipole orientations and intermolecular distances (Figs. S9–S12). The electronic band structure of this (BCB)<sub>n</sub> chain (Fig. S13) shows characteristics similar to that of BBCBB (Fig. S6) but with a much larger dispersion. In particular it leads to 0.17 electrons in the (BCB)<sub>n</sub> related conduction band near the X' and K" points (and a corresponding number of holes in the valence band near the  $\Gamma$  point). However, this (BCB)<sub>n</sub> configuration no longer has prefers the 2nd bi-layer, as shown in Fig. S14. Rather it prefers to be far from the surface, in the bulk.

Although the t-t-BBCBB tetramer has a singlet ground state (S=0) at -0.96 eV, the excited triplet state (S=1) at -0.32 eV is more stable than most other species. It could possibly play a role in forming the Cooper

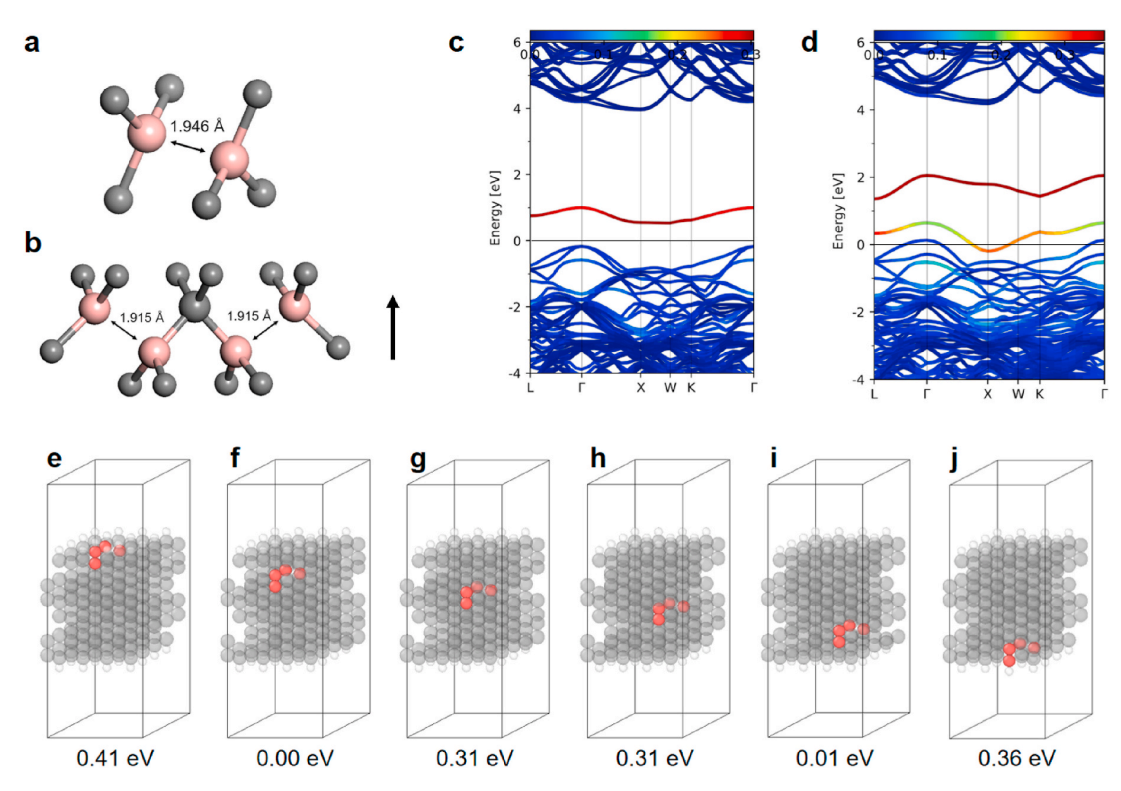


Fig. 6. Schematic structures for a) BB (1.6 at%) and b) t-t-BBCBB (3.1 at%) complexes. Grey and pink spheres represent C and B, respectively. The electric dipole direction of t-t-BBCBB is shown in b) with an arrow. The predicted electronic band structure and density of states (DOS) are shown in (c) for the BB dimer and in (d) for the t-t-BBCBB defect. The color represents the Boron contribution to a band (red  $\rightarrow$  100 % B). (e-j) The relative energies depending on the t-t-BBCBB depth which is parallel with the H-terminated diamond (111) surface in a slab model of 4x4 surface unit cell with 6 bilayers (228 atoms). The BBCBB defect located in the second bi-layer beneath the surface is the most favorable. Note that (h), (i), and (j) correspond to (g), (f), and (e), respectively, with the BBCBB dipole orientations reversed towards the (111) facet.

pairs of the superconducting state [57], perhaps explaining the bosonic anomalies observed in superconductivity [58].

#### 3.4. Boron tetramers influence on superconductivity anisotropy

Based on our measurements and quantum mechanics calculations, we conclude that the appearance of an anomalous resistance peak in the  $R_{YY}$  direction may result from two interaction cases. First, as illustrated in Fig. 7a the BBCBB dimers form the pillar-like structure in the  $R_{XX}$  direction, which corresponds to clear transition to superconductivity.

This creates a conduction highways in the  $R_{XX}$  direction. But in the  $R_{YY}$  direction, the path for electrical charge transfer is longer, which leads to a difference in coherence length between  $R_{XX}$  and  $R_{YY}$ .

The calculated coherence length from equations (2) and (3) for Configuration I ( $R_{XX}$ ) is equal to 12.8 nm. In contrast the coherence length for Configuration II ( $R_{YY}$ ) is significant larger, reaching 34.4 nm. This almost three times increase in the coherence length suggests the formation of bosonic cooper-like pairs. Based on our observations, we attribute the varying boron concentration for  $R_{XX}$  and  $R_{YY}$  to the absorption of differing quantities of boron at the different diamond facets

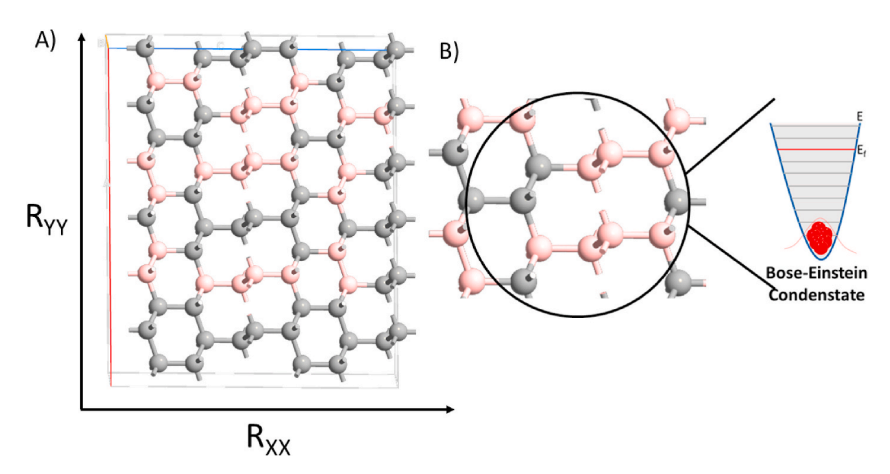


Fig. 7. A) Pillar-like structure of BBCBB dimer in diamond supercell and B) the interaction of BBCBB dimers to form the Bose-Einstein condensate.

at the microscopic level. We find experimentally that the (111) facet absorbs ten times more boron than the (100) facet for the same level of boron doping [59], which agrees with literature data [7,60,61], making t-t-BBCBB to be form easily along the (111) facet.

$$\mu_0 H_{c2} = -A T_c \frac{d\mu_0 H_{c2}}{dT} \bigg| T = T_c \tag{2}$$

$$H_{c2} = \Phi_0 / 2\pi \xi_{GL}^2 \tag{3}$$

A similar asymmetry phenomena has been observed in non-homogeneous doped and un-doped granular superconductors, like granular Al films and wires [62], granular silver doped Au films [63], disordered Cu-Zn alloys [64], disordered Nb antidot arrays [65], La<sub>2-x</sub>. Ce<sub>x</sub>CuO<sub>4</sub> single crystals [66], and high-temperature cuprate superconductors when measured in the out-of-plane direction [67]. In cuprates the superconducting Cu-O planes are separated by layers that are essentially insulating. Since the coherence length in cuprates is tiny ( $\sim$ 1 nm or less) and anisotropic (much smaller in the c direction) a separation of just a few angstroms between the SC planes is sufficient to produce the effect that we observe in BDD on the nanometer scale. The stacking of the BBCBB tetramers in BDD may lead high transport in the stacking direction, but low transport in the perpendicular direction. Thus, these asymmetries may be related to our observed surface conductively asymmetry for BDD.

Secondly, as shown in Fig. 7b the interaction of the boron dimers (to form tetramers) is responsible for the bosonic anomaly, which results in an anomalous resistance peak. As illustrated in Fig. 5a, at temperatures above T<sub>c</sub> (2.4K) the resistivity shows semiconducting behavior, but below Tc, there is a transition to the superconducting state. In contrast Fig. 7b illustrates that as the temperature decreases a Bose-Einstein condensate can form due the nature of BBCBB dimer, which counts as a boson (S = 0, see Table 2). According to work by Keilmann and Tassilo [57] the Bosonic Cooper-like pairs, which can be created dynamically, form pairs of long-range bosons that lead to entangled states, instead of being attractive these entangled bosons states behave as local insulators. Due to filled and paired outer shell electrons, diamond has virtually no magnetic response other than quantum mechanical diamagnetism. This is visible in our data (see Fig. 6) above 2.2-2.3K, where there is no response to the applied external magnetic field. Below 2.2-2.3K, superconducting cooper pair droplets start to form and for configuration I the sample becomes strongly diamagnetic. Assuming that Cooper pairs are formed, they may not necessarily overlap within the coherence length. This would increase the resistance, leading to paramagnetic behavior in configuration II [68]. This can be explained by formation of Cooper pair droplets into a bosonic insulating phase (before a full superconducting liquid is formed), but it could well arise from proximity to the metal-insulator transition (in terms of dopant concentration and boron-tetramers).

Considering that a resistive superconducting transition is a process in which Cooper pairs take over control of electrical transport from single quasiparticles, G. Zhang et al. reports that bosonic anomalies in boron doped diamond can lead to an anomalous resistance peak that can be interpreted in terms of confinement and coherence effects in the presence of intrinsic and extrinsic granularity [12].

# 4. Summary and conclusions

We prepared boron-doped diamond thin films using Microwave Plasma Assisted Chemical Vapor Deposition with a deuterium-rich plasma. We find an anomalous phase transition linked with the emergence of boson quantum entanglement states behaving as a bosonic insulating state. We demonstrate that the superconducting properties of the diamond film are anisotropic, which might enable applications such as single-photon detectors based on the formation of superconducting nanowire structures within the material [69].

We use quantum mechanics at the DFT level to predict the states formed by B dopants. We find that isolated B sites prefer to form BB dimers and that a pair of dimers strongly prefers to aggregate to form the t-t-BBCBB cluster oriented along a  $<\!110>$  direction. We find that the t-t-BBCBB defect leads to metallic character (Mott Metal-insulator transition) with holes in the valence band near the  $\Gamma$  point and electrons in a BBCBB promoted band near the K point edge. Thus, we predict that the t-t-BBCBB configuration is responsible for the Mott Metal-Insulator Transition and presumably the superconductivity. These BBCBB clusters prefer to have their  $<\!110>$  axis parallel to the (111) surface, lying in the 2nd double layer just below the D-terminated surface double layer.

The interaction of the boron dimers or tetramers may lead to the bosonic anomaly, which is responsible for the anomalous resistance peak. However, the amount of boron doping will be different in different facets and the granular nature of the  $\mbox{BDD}_{\mbox{\scriptsize D}}$  may also contribute to the anomalous resistance peak.

### CRediT authorship contribution statement

Michał Sobaszek: Writing – original draft, Visualization, Validation, Supervision, Methodology, Investigation, Formal analysis, Conceptualization. Soonho Kwon: Writing – original draft, Visualization, Investigation, Formal analysis. Tomasz Klimczuk: Writing – original draft, Investigation, Formal analysis. Paweł P. Michałowski: Data curation, Formal analysis, Writing – original draft, Investigation, Formal analysis. Bogdan Rutkowski: Writing – original draft, Investigation. Formal analysis. Bogdan Rutkowski: Writing – original draft, Investigation. Dongying Wang: Investigation. Xinwei Linvestigation. Marc Bockrath: Writing – review & editing, Project administration, Investigation, Formal analysis. Robert Bogdanowicz: Writing – review & editing, Supervision, Project administration. William A. Goddard: Writing – review & editing, Writing – original draft, Supervision, Project administration, Investigation, Formal analysis.

#### Declaration of competing interest

The authors declare that they have no known competing financial interests or personal relationships that could have appeared to influence the work reported in this paper.

#### Acknowledgements

W.A.G acknowledges support from the NSF (CBET-2311117); this work used the Extreme Science and Engineering Discovery Environment (XSEDE) for DFT calculations, which is supported by the NSF grant number ACI-1548562; S.K. acknowledges support from the Resnick Sustainability Institute at Caltech. R.B. acknowledges the support of these studies from Gdańsk University of Technology by the DEC-12/2023/IDUB/IV.2/EUROPIUM grant under the Europium Short-Term Outgoing Visits - 'Excellence Initiative - Research University' program. P.P.M. was supported by the National Centre for Research and Development, Poland, project No. LIDER/8/0055/L-12/20/NCBR/2021.

### Appendix A. Supplementary data

Supplementary data to this article can be found online at https://doi.org/10.1016/j.carbon.2024.119337.

#### References

- [1] E. Bustarret, P. Achatz, B. Sacépé, C. Chapelier, C. Marcenat, L. Ortéga, T. Klein, Phil. Trans. Math. Phys. Eng. Sci. 366 (2008) 267.
- [2] N. Dubrovinskaia, G. Eska, G.A. Sheshin, H. Braun, J. Appl. Phys. 99 (2006) 033903
- [3] Z.L. Wang, Q. Luo, L.W. Liu, C.Y. Li, H.X. Yang, H.F. Yang, J.J. Li, X.Y. Lu, Z.S. Jin, L. Lu, C.Z. Gu, Diam. Relat. Mater. 15 (2006) 659.
- L. Lu, C.Z. Gu, Diam. Relat. Mater. 15 (2006) 659.
  [4] G.M. Klemencic, J.M. Fellows, J.M. Werrell, S. Mandal, S.R. Giblin, R.A. Smith, O. A. Williams, Phys. Rev. Mater. 1 (2017) 044801.

- [5] M. Nesládek, D. Tromson, C. Mer, P. Bergonzo, P. Hubik, J.J. Mares, Appl. Phys. Lett. 88 (2006) 232111.
- [6] W. Gajewski, P. Achatz, O.A. Williams, K. Haenen, E. Bustarret, M. Stutzmann, J. A. Garrido, Phys. Rev. B 79 (2009) 045206.
- [7] Y. Takano, M. Nagao, T. Takenouchi, H. Umezawa, I. Sakaguchi, M. Tachiki, H. Kawarada, Diam. Relat. Mater. 14 (2005) 1936.
- [8] G. Zhang, S.D. Janssens, J. Vanacken, M. Timmermans, J. Vacík, G.W. Ataklti, W. Decelle, W. Gillijns, B. Goderis, K. Haenen, P. Wagner, V.V. Moshchalkov, Phys. Rev. B 84 (2011) 214517.
- [9] Ya M. Blanter, V.M. Vinokur, L.I. Glazman, Phys. Rev. B 73 (2006) 165322.
- [10] I.V. Lerner, A.A. Varlamov, V.M. Vinokur, Phys. Rev. Lett. 100 (2008) 117003. [11] G.M. Klemencic, D.T.S. Perkins, J.M. Fellows, C.M. Muirhead, R.A. Smith
- S. Mandal, S. Manifold, M. Salman, S.R. Giblin, O.A. Williams, Carbon 175 (2021)
- [12] G. Zhang, T. Samuely, J. Kačmarčík, E.A. Ekimov, J. Li, J. Vanacken, P. Szabó, J. Huang, P.J. Pereira, D. Cerbu, V.V. Moshchalkov, Phys. Rev. Appl. 6 (2016)
- [13] P. Ashcheulov, J. Šebera, A. Kovalenko, V. Petrák, F. Fendrych, M. Nesládek, A. Taylor, Z. Vlčková Živcová, O. Frank, L. Kavan, M. Dračínský, P. Hubík, J. Vacík, I. Kraus, I. Kratochvílová, Eur. Phys. J. B 86 (2013) 443.
- [14] G. Zhang, T. Samuely, N. Iwahara, J. Kačmarčík, C. Wang, P.W. May, J.K. Jochum, O. Onufriienko, P. Szabó, S. Zhou, P. Samuely, V.V. Moshchalkov, L.F. Chibotaru, H.-G. Rubahn, Sci. Adv. 6 (2020) eaaz2536.
- [15] G. Zhang, J. Kačmarčík, Z. Wang, R. Zulkharnay, M. Marcin, X. Ke, S. Chiriaev, V. Adashkevich, P. Szabó, Y. Li, P. Samuely, V.V. Moshchalkov, P.W. May, H.-G. Rubahn, Phys. Rev. Appl. 12 (2019) 064042.
- [16] R. Bogdanowicz, M. Sobaszek, M. Sawczak, G.M. Grigorian, M. Ficek, P. Caban, A. Herman, A. Cenian, Diam. Relat. Mater. 96 (2019) 198.
- [17] K. Schwarzová-Pecková, J. Vosáhlová, J. Barek, I. Šloufová, E. Pavlova, V. Petrák, J. Zavázalová, Electrochim. Acta 243 (2017) 170.
- [18] P. Ashcheulov, J. Šebera, A. Kovalenko, V. Petrák, F. Fendrych, M. Nesládek, A. Taylor, Z. Vlčková Živcová, O. Frank, L. Kavan, M. Dračínský, P. Hubík, J. Vacík,
- I. Kraus, I. Kratochvílová, Eur. Phys. J. B 86 (2013) 443. [19] L. Niu, J.-Q. Zhu, X. Han, M.-L. Tan, W. Gao, S.-Y. Du, Phys. Lett. 373 (2009) 2494.
- [20] X. Blase, Ch Adessi, D. Connétable, Phys. Rev. Lett. 93 (2004) 237004.
- [21] P.P. Michałowski, M. Anayee, T.S. Mathis, S. Kozdra, A. Wójcik, K. Hantanasirisakul, I. Jóźwik, A. Piątkowska, M. Możdżonek, A. Malinowska, R. Diduszko, E. Wierzbicka, Y. Gogotsi, Nat. Nanotechnol. 17 (2022) 1192.
  [22] G. Kresse, J. Hafner, Phys. Rev. B 49 (1994) 14251.
  [23] G. Kresse, J. Furthmüller, Phys. Rev. B 54 (1996) 11169.

- [24] J.P. Perdew, K. Burke, M. Ernzerhof, Phys. Rev. Lett. 77 (1996) 3865.
- [25] E.R. Johnson, A.D. Becke, J. Chem. Phys. 124 (2006) 174104.
- [26] P.E. Blöchl, Phys. Rev. B 50 (1994) 17953.
- [27] H.J. Monkhorst, J.D. Pack, Phys. Rev. B 13 (1976) 5188.
- [28] J.W. Ager, W. Walukiewicz, M. McCluskey, M.A. Plano, M.I. Landstrass, Appl. Phys. Lett. 616 (1995) 616.
- [29] P. Gonon, E. Gheeraert, A. Deneuville, F. Fontaine, L. Abello, G. Lucazeau, J. Appl. Phys. 78 (1995) 7059.
- [30] V. Mortet, Z.V. Živcová, A. Taylor, M. Davydová, O. Frank, P. Hubík, J. Lorincik, M. Aleshin, Diam. Relat. Mater. 93 (2019) 54.
- [31] E. Bustarret, E. Gheeraert, K. Watanabe, Phys. Status Solidi 199 (2003) 9.
- [32] M. Bernard, A. Deneuville, P. Muret, Diam. Relat. Mater. 13 (2004) 282.
- [33] V. Mortet, Z.V. Živcová, A. Taylor, M. Davydová, O. Frank, P. Hubík, J. Lorincik, M. Aleshin, Diam. Relat. Mater. 93 (2019) 54.
- [34] M. Sobaszek, M. Brzhezinskaya, A. Olejnik, V. Mortet, M. Alam, M. Sawczak, M. Ficek, M. Gazda, Z. Weiss, R. Bogdanowicz, Small 19 (2023) 2208265.
- V. Mortet, I. Gregora, A. Taylor, N. Lambert, P. Ashcheulov, Z. Gedeonova, P. Hubik, Carbon S0008622320306448, 2020. [35]
- [36] W. Gajewski, P. Achatz, O.A. Williams, K. Haenen, E. Bustarret, M. Stutzmann, J. A. Garrido, Phys. Rev. B 79 (2009) 045206.
- [37] K. Ushizawa, K. Watanabe, T. Ando, I. Sakaguchi, M. Nishitani-Gamo, Y. Sato, H. Kanda, Diam. Relat. Mater. 7 (1998) 1719.
- [38] J.V. Macpherson, Phys. Chem. Chem. Phys. 17 (2015) 2935.

- [39] M. Ficek, K.J. Sankaran, J. Ryl, R. Bogdanowicz, I.-N. Lin, K. Haenen, K. Darowicki, Appl. Phys. Lett. 108 (2016) 241906.
- K.J. Sankaran, M. Ficek, K. Panda, C.-J. Yeh, M. Sawczak, J. Ryl, K.-C. Leou, J. Y. Park, I.-N. Lin, R. Bogdanowicz, K. Haenen, ACS Appl. Mater. Interfaces 11 (2019) 48612.
- [41] H.M. Fernández, D. Rogler, G. Sauthier, M. Thomasset, R. Dietsch, V. Carlino, E. Pellegrin, Sci. Rep. 8 (2018) 1.
- [42] W. Shen, H. Li, C. Wang, Z. Li, Q. Xu, H. Liu, Y. Wang, J. Mater. Chem. A 3 (2015) 15190
- [43] M. Belyansky, M. Trenary, C. Ellison, Surf. Sci. Spectra 3 (1994) 147.
- [44] J. Ryl, L. Burczyk, R. Bogdanowicz, M. Sobaszek, K. Darowicki, Carbon 96 (2016)
- [45] J. Ryl, A. Zielinski, R. Bogdanowicz, K. Darowicki, Electrochem. Commun. 83 (2017)41.
- [46] Yu V. Pleskov, Yu E. Evstefeeva, M.D. Krotova, V.P. Varnin, I.G. Teremetskaya, J. Electroanal. Chem. 595 (2006) 168.
- [47] P.P. Michałowski, J. Müller, C. Rossi, A. Burenkov, E. Bär, G. Larrieu, P. Pichler, Measurement 211 (2023) 112630.
- [48] P.P. Michałowski, J. Anal. At. Spectrom. 34 (2019) 1954.
- [49] G. Zhang, S.D. Janssens, J. Vanacken, M. Timmermans, J. Vacík, G.W. Ataklti, W. Decelle, W. Gillijns, B. Goderis, K. Haenen, P. Wagner, V.V. Moshchalkov, Phys. Rev. B 84 (2011) 214517.
- [50] J.J. Mareš, M. Nesládek, P. Hubík, D. Kindl, J. Krištofik, Diam. Relat. Mater. 16 (2007)1
- [51] B.L. Willems, G. Zhang, J. Vanacken, V.V. Moshchalkov, S.D. Janssens, K. Haenen, P. Wagner, J. Phys. D Appl. Phys. 43 (2010) 374019.
- [52] P. Achatz, E. Bustarret, C. Marcenat, R. Piquerel, T. Dubouchet, C. Chapelier, A. M. Bonnot, O.A. Williams, K. Haenen, W. Gajewski, J.A. Garrido, M. Stutzmann, Phys. Status Solidi 206 (2009) 1978.
- [53] G. Zhang, T. Samuely, J. Kačmarčík, E.A. Ekimov, J. Li, J. Vanacken, P. Szabó, J. Huang, P.J. Pereira, D. Cerbu, V.V. Moshchalkov, Phys. Rev. Appl. 6 (2016) 064011.
- [54] M. Abdel-Hafiez, D. Kumar, R. Thiyagarajan, Q. Zhang, R.T. Howie, K. Sethupathi, O. Volkova, A. Vasiliev, W. Yang, H.K. Mao, M.S.R. Rao, Phys. Rev. B 95 (2017) 174519.
- [55] X. Liu, X. Chen, D.J. Singh, R.A. Stern, J. Wu, S. Petitgirard, C.R. Bina, S D. Jacobsen, Proceedings of, 116, the National Academy of Sciences, 2019, n. 7703.
- [56] L. Niu, J.-O. Zhu, X. Han, M.-L. Tan, W. Gao, S.-Y. Du, Phys. Lett. 373 (2009) 2494.
- [57] T. Keilmann, J.J. García-Ripoll, Phys. Rev. Lett. 100 (2008) 110406.
- G. Zhang, T. Samuely, H. Du, Z. Xu, L. Liu, O. Onufriienko, P.W. May, J. Vanacken, P. Szabó, J. Kačmarčík, H. Yuan, P. Samuely, R.E. Dunin-Borkowski, J. Hofkens, V. V. Moshchalkov, ACS Nano 11 (2017) 11746.
- [59] K. Ushizawa, K. Watanabe, T. Ando, I. Sakaguchi, M. Nishitani-Gamo, Y. Sato, H. Kanda, Diam. Relat. Mater. 7 (1998) 1719.
- [60] T. Klein, P. Achatz, J. Kacmarcik, C. Marcenat, F. Gustafsson, J. Marcus, E. Bustarret, J. Pernot, F. Omnes, B.E. Sernelius, C. Persson, A. Ferreira da Silva, C. Cytermann, Phys. Rev. B 75 (2007) 165313.
- [61] K. Winzer, D. Bogdanov, Ch Wild, Physica C (Amsterdam, Neth.) 432 (2005) 65.[62] M. Park, M.S. Isaacson, J.M. Parpia, Phys. Rev. B 55 (1997) 9067.
- [63] P.S. Mahapatra, S.K. Saha, R. Mahadevu, S. Islam, P. Mondal, S. Kumbhakar, T.P. Sai, S. Patil, U. Chandni, A. Pandey, A. Ghosh, Observation of excess resistance anomaly at resistive transitions in Ag/Au nanostructures, (2019). http://arxiv. org/abs/1912.05428 (accessed August 17, 2022).
- [64] P. Lindqvist, A. Nordström, Ö. Rapp, Phys. Rev. Lett. 64 (1990) 2941.
- [65] J. Hua, Z.L. Xiao, D. Rosenmann, I. Beloborodov, U. Welp, W.K. Kwok, G. W. Crabtree, Appl. Phys. Lett. 90 (2007) 072507.
- [66] M.A. Crusellas, J. Fontcuberta, S. Piñol, Phys. Rev. B 46 (1992) 14089.
- [67] G. Heine, W. Lang, X.L. Wang, S.X. Dou, Phys. Rev. B 59 (1999) 11179.
- [68] D. Mtsuko, C. Coleman, S. Bhattacharyya, EPL 124 (2019) 57004.
- [69] I. Esmaeil Zadeh, J. Chang, J.W.N. Los, S. Gyger, A.W. Elshaari, S. Steinhauer, S. N. Dorenbos, V. Zwiller, Appl. Phys. Lett. 118 (2021) 190502.